

See discussions, stats, and author profiles for this publication at: <https://www.researchgate.net/publication/229432588>

The Ferroic Phase Transitions of BiFeO₃

ARTICLE *in* ADVANCED MATERIALS · OCTOBER 2008

Impact Factor: 17.49 · DOI: 10.1002/adma.200800218

CITATIONS

79

READS

168

4 AUTHORS, INCLUDING:



[Sverre M. Selbach](#)

Norwegian University of Science and Techn...

35 PUBLICATIONS 757 CITATIONS

SEE PROFILE



[Thomas Tybell](#)

Norwegian University of Science and Techn...

96 PUBLICATIONS 2,082 CITATIONS

SEE PROFILE



[Mari-Ann Einarsrud](#)

Norwegian University of Science and Techn...

202 PUBLICATIONS 3,215 CITATIONS

SEE PROFILE

The Ferroic Phase Transitions of BiFeO₃**

By Sverre M. Selbach, Thomas Tybell, Mari-Ann Einarsrud, and Tor Grande*

Multiferroics^[1] have rapidly gained increasing attention due to a wide range of potential applications^[2] in microelectronic and spintronic devices, and the possibility of controlling magnetic order by electric fields,^[3] or vice versa,^[4] through magnetoelectric coupling.^[5] BiFeO₃ is termed a multiferroic material due to coexistence of ferroelasticity, antiferromagnetism, and ferroelectricity.^[6–8] A large spontaneous polarization^[9–11] P_s of 88–100 $\mu\text{C cm}^{-2}$ and a high T_C of 830 °C makes the material a prime candidate for lead-free ferroelectric memories. Antiferromagnetic ordering is G-type and $T_N = 370$ °C.^[7] Magnetoelectric bismuth ferrite is the hitherto only compound known to combine ferroelectric and magnetic ordering above room temperature, and is the most extensively studied multiferroic material. Ambient properties of thin films have been extensively investigated,^[9,12] but studies of the ferroic phase transitions are scarce. Here, we report on the two ferroic phase transitions of BiFeO₃ at T_N and T_C .

BiFeO₃ is a rhombohedrally distorted perovskite. In terms of symmetry the space group is $R3c$ with hexagonal lattice parameters $a_{\text{hex}} = 5.58$ Å and $c_{\text{hex}} = 13.87$ Å (rhombohedral $a_{\text{rh}} = 5.63$ Å, $\alpha_{\text{rh}} = 59.35^\circ$) at ambient temperature.^[6,7] Valuable insight to the low temperature properties has been provided by first principles calculations,^[9–11] but there is no corresponding understanding of the high temperature behavior. Structure analysis based on high temperature diffraction data have previously been reported up to 650 °C.^[13] However, the presence of secondary phases^[14] Bi₂₅FeO₃₉ and Bi₂Fe₄O₉ may hamper the structural characterization of the paraelectric phase above the high T_C of 830 °C. The nature of the ferroelectric transition of BiFeO₃ and its paraelectric structure has thus not yet conclusively been identified, although cubic $Pm\bar{3}m$, rhombohedral $R3m$, orthorhombic $P2mm$, and tetragonal $I4/mcm$ have been suggested.^[15–18] In this communication we provide experimental evidence that the crystal

structure of the high temperature paraelectric phase is centrosymmetric $R\bar{3}c$. The ferroelectric transition is first order and accompanied by discontinuous volume and abrupt changes in atomic positions. A continuous lattice anomaly is associated with the second order magnetic phase transition at T_N . Electrical conductivity anomalies associated with both phase transitions are observed. The present findings provide a basis for fundamental insight to the multiferroic properties.

The two ferroic phase transitions, from the ferroelectric to the paraelectric state at $T_C = 830$ °C, and between antiferromagnetism and paramagnetism at $T_N = 370$ °C (inset), respectively, are both evident from calorimetric measurements in Figure 1. The transition temperatures are in good accordance with previous reports.^[7,19] T_N and T_C are identical for a BiFeO₃ bulk powder and a monolithic polycrystalline sample. The enthalpy associated with the ferroelectric transition is approximately 10 times that of the magnetic, and they were measured to be 0.3 ± 0.03 and 3 ± 0.3 kJ mol^{−1}, respectively. The substantially different enthalpies $\Delta_{\text{trs}}H$ involved in the two transitions reflect the microscopic nature and thermodynamic order of the transitions, the ferroelectric being first order, evidenced by thermal hysteresis, and the magnetic second order.

Normalized lattice parameters $a = 2^{-1/2} a_{\text{hex}}$ and $c = 12^{-1/2} c_{\text{hex}}$ in the vicinity of T_N are shown in Figure 2b. c is larger than a due to the unit cell elongation parallel to $P_s || c_{\text{hex}}$, while $c = a$ would correspond to an ideal cubic perovskite. The magnetic transition is associated with anomalous lattice expansion, explaining early reports of a volume discontinuity at T_N .^[20] However, dilatometry of a dense polycrystal (Fig. 2b) confirmed that the volume is continuous through the magnetic transition, revealing the second order nature of the phase transition in line with the observed discontinuity of the thermal expansion coefficient (not shown). Spontaneous polarization arises from polar displacements of cations along the $[001]_{\text{hex}} || [111]_{\text{rh}}$ axis, represented by parameters^[21] s and t for Bi³⁺ and Fe³⁺, respectively (Fig. 2a). Antiferrodistortive rotation of oxygen octahedra, ω , are about the $[001]_{\text{hex}}$ axis. ω is linked to the displacement parameters d and e for O^{2−} from its ideal position ($1/6 - 2e - 2d$, $1/3 - 4d$, and $1/12$), by $2e3^{1/2} \tan \omega$.^[21] We have previously proposed cooperative cation displacements, s – t , as a crystallographic order parameter linked to P_s .^[22] No anomalies in pseudotetragonality c/a , cooperative cation displacements s – t (Fig. 2c) or rotation of oxygen octahedra (Fig. 2d) were evident through the magnetic transition within the uncertainty of the structure refinement. The anomalous increase in unit cell volume is consistent with observations of decreasing wave numbers for certain Raman modes in the vicinity of T_N .^[15] The close-to-isotropic lattice

[*] Prof. T. Grande, Prof. M.-A. Einarsrud, S. M. Selbach
Department of Materials Science and Engineering
Norwegian University of Science and Technology (NTNU)
7491 Trondheim (Norway)
E-mail: tor.grande@material.ntnu.no

Prof. T. Tybell
Department of Electronics and Telecommunications
Norwegian University of Science and Technology (NTNU)
7491 Trondheim (Norway)

[**] Elin Nilsen and Espen Rudberg at NTNU are acknowledged for assisting HTXRD and conductivity measurements, respectively. This work was supported by the Norwegian University of Science and Technology and the Research Council of Norway (NANOMAT, grants 158518/431, 140553/130, and 162874/V00). Supporting Information is available online from Wiley InterScience or from the authors.

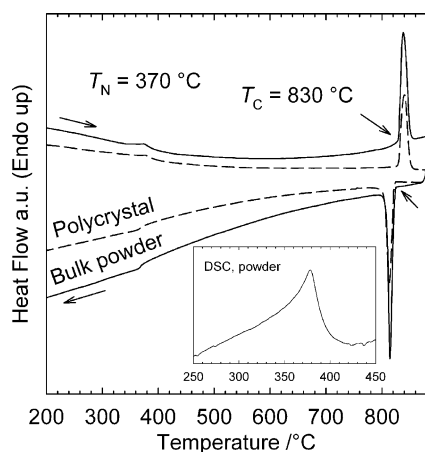


Figure 1. Differential thermal analysis traces demonstrate the significantly different amounts of enthalpy involved in the antiferromagnetic (370 °C) and ferroelectric (830 °C) transitions. Inset: differential scanning calorimetric trace showing the lambda-shape of the calorimetric trace for the antiferromagnetic phase transition. Arrows denote the transition temperatures as the peak temperature of the magnetic transition, and the onset temperature of the ferroelectric transition.

expansion associated with G-type antiferromagnetic ordering in BiFeO₃ as shown here is in contrast with the behavior of multiferroic YMnO₃.^[23] In YMnO₃ A-type antiferromagnetic ordering at $T_N = 76$ K is accompanied by contraction in the a - b plane and expansion along the c axis, resulting in a net volume contraction. It should be noted that unlike BiFeO₃, ferroelectricity in YMnO₃ is geometrically driven.^[24]

We now turn our attention to the paraelectric crystal structure of BiFeO₃. The ferroelectric structure $R3c$ is related to the ideal perovskite structure $Pm\bar{3}m$ by freezing in two different crystal distortions. Polar displacements s and t of Bi³⁺ and Fe³⁺, respectively along $[001]_{\text{hex}}$ reduces the symmetry to the polar space group $R3m$. Antiferrodistortive rotation of the oxygen octahedra about the $[001]_{\text{hex}}$ axis alone yields the nonpolar space group $R\bar{3}c$. $R3c$ results from the combination of these two distortions. To identify the space group of the paraelectric phase we have applied selection rules^[25] for perovskites to the X-ray diffractograms acquired above T_C . The $(113)_{\text{hex}}$, $(006)_{\text{hex}}$, and $(202)_{\text{hex}}$ reflections (Fig. 3) are chosen for illustration. The $(006)_{\text{hex}}$ and $(202)_{\text{hex}}$ reflections are clearly resolved both below and above T_C , note that the splitting of individual Bragg reflections is due to the Cu $K\alpha_1$ and α_2 contributions. Resolved $(006)_{\text{hex}}$ and $(202)_{\text{hex}}$ reflections at 872 and 926 °C exclude the possibility of a cubic space group, where these reflections would have merged to a single (111) reflection. The $(113)_{\text{hex}}$ reflection is due to oxygen planes caused by antiferrodistortive rotation of oxygen octahedra in the Glazer tilt system^[26] $a^-a^-a^-$, and thus low in intensity. This reflection prevails through the ferroelectric transition, implying that the tilt system does not change at T_C . The resolved $(006)_{\text{hex}}$ and $(202)_{\text{hex}}$ reflections and the $(113)_{\text{hex}}$ reflection unambiguously identifies the paraelectric space group as

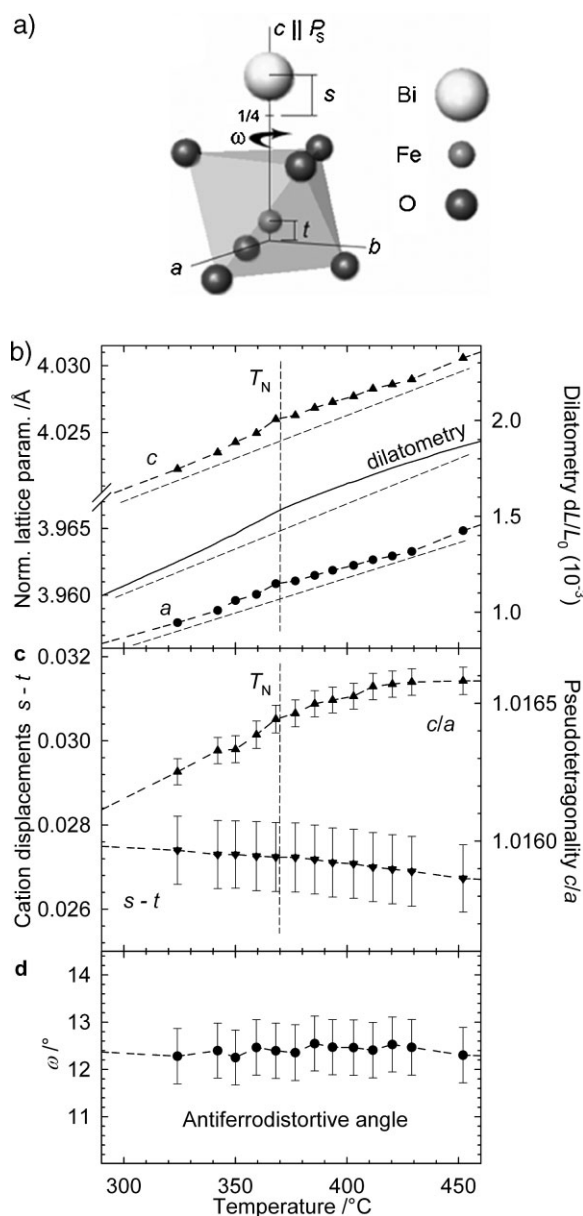


Figure 2. Crystallographic properties across the antiferromagnetic phase transition at 370 °C. a) Illustration of the $R3c$ structure with hexagonal axes. Displacements s and t of Bi³⁺ and Fe³⁺, respectively, are along the $[001]_{\text{hex}}$ axis. $s > t$ and cooperative cation displacements, $s-t$, is a crystallographic measure of polarization. Antiferrodistortive rotation ω of oxygen octahedra is about the $[001]_{\text{hex}}$ axis. b) Normalized lattice parameters and thermal expansion (dilatometric trace). Dashed lines are guides to the eye. c) Pseudotetragonality c/a and cooperative cation displacements $s-t$. d) Antiferrodistortive rotation ω . Refinement uncertainties are smaller than the symbols if not shown.

centrosymmetric $R\bar{3}c$. Previous space groups suggested for paraelectric BiFeO₃ can thus be ruled out. Possessing the $a^-a^-a^-$ tilt system also above T_C , the paraelectric phase is expected to be ferroelastic, in concordance with isostructural LaCoO₃.^[27] BiFeO₃ is known to be unstable at elevated

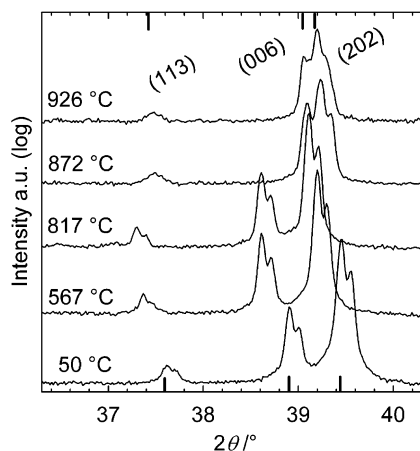


Figure 3. Identification of the paraelectric phase by high temperature X-ray diffraction. Diffractograms are shown for selected temperatures, focusing on the Bragg reflections distinguishing possible paraelectric structures above T_C . Refined positions of Bragg reflections at 50 and 926 °C are shown as ticks at the bottom and top axes, respectively.

temperatures, and some weak reflections from decomposition to $\text{Bi}_2\text{Fe}_4\text{O}_9$ and $\text{Bi}_{25}\text{FeO}_{39}$ are present at 872 and 926 °C outside the 2θ range shown in Figure 3. HTXRD using a BiFeO_3 powder sample prepared by a chemical route^[22] confirmed the previous observation and we conclude that $R\bar{3}c$ is the paraelectric space group above T_C .

Lattice parameters and primitive unit cell volume (Fig. 4a) display nonlinear thermal evolution from room temperature in accordance with reports up to 650 °C.^[1,3] The unit cell volume abruptly decreases by $\sim 1.4\%$ from 64.0 \AA^3 at 817 °C to 63.1 \AA^3

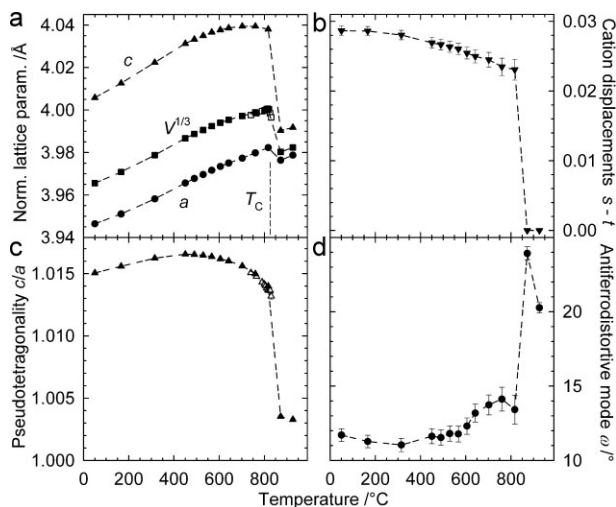


Figure 4. Crystallographic features of the ferroelectric phase transition. a) Normalized lattice parameters. Open symbols are additional measurements close to T_C . b) The crystallographic order parameter, cooperative cation displacements $s-t$. c) Pseudotetragonality c/a . d) Antiferrodistortive rotation ω of oxygen octahedra.

at 872 °C through the ferroelectric transition. The $R\bar{3}c$ to $R3c$ transition requires only that the cations are displaced by s and t from their centrosymmetric positions. A second order transition would be allowed in terms of symmetry groups and subgroups, but the discontinuous volume at T_C (Fig. 4a), the significant enthalpy of the transition and the thermal hysteresis (Fig. 1) unambiguously identifies the transition as first order.

The cooperative cation displacements, $s-t$, related to polarization, qualitatively follows the expected behavior of an order parameter for a ferroelectric transition (Fig. 4b), although the finite value of $s-t$ is still 80% of the value at ambient temperature even at 817 °C before becoming zero in paraelectric $R\bar{3}c$. The unit cell distortion, represented by pseudotetragonality c/a , increases with temperature up to a maximum close to 450 °C, followed by a continuous decrease toward T_C , and a discontinuous reduction through the ferroelectric transition, as shown in Figure 4c. Extrapolation of the thermal evolution of c/a of the paraelectric BiFeO_3 to unity predicts a phase transition to $Pm\bar{3}m$ far above the peritectic decomposition temperature at 934–961 °C.^[16,17] Antiferrodistortive rotation ω of the oxygen octahedra (Fig. 4d) does not decrease upon approaching T_C , but increases anomalously across T_C . Lattice contraction is the plausible cause of the anomalous enhancement of ω at T_C . Structural nonlinearity with respect to c/a and ω above 450 °C may be related to the loss of spin-lattice coupling in the paramagnetic phase. Our observations of a discontinuous increase in ω at T_C , and the prediction of a ferroelastic transition to $Pm\bar{3}m$ above the decomposition temperature, are both qualitatively consistent with recent Monte Carlo simulations, which also predicts an intermediate paraelectric, ferroelastic structure with large ω , and a transition to $Pm\bar{3}m$ at $\sim 1440 \text{ K}$.^[18] The abrupt decrease of $s-t$ at T_C suggests incomplete mode softening and a displacive model for the first order ferroelectric transition. Incomplete mode softening has also been found by experimental^[28] and theoretical^[29] studies of phonon spectra. An analogy can be drawn to the $R3c$ to $R\bar{3}c$ ferroelectric transitions of LiNbO_3 and LiTaO_3 , where soft mode damping is observed far from T_C , but a crossover to order–disorder nature occurs close to T_C .^[30] However, the large $\Delta_{\text{trs}}V$ and $\Delta_{\text{trs}}H$ reported here distinguish BiFeO_3 from LiNbO_3 and LiTaO_3 . From the present study it is not possible to conclusively determine whether the cations are located at the centrosymmetric positions in $R\bar{3}c$ (displacive model) or thermally averaged at the centrosymmetric sites as in the eight-site model^[31] for an order–disorder transition. Incomplete mode softening, large $\Delta_{\text{trs}}H$ and $\Delta_{\text{trs}}V$ points to a mainly displacive character of the phase transition.

The electrical conductivity of dense polycrystalline BiFeO_3 increases continuously from 300 °C to T_C at 830 °C, giving further evidence for no structural transitions at the Néel temperature (Fig. 5a). A conductivity hysteresis associated with the first order ferroelectric transition is evident in the inset of Figure 5a. The steep rise in conductivity at T_C mirrors the structural differences between the ferroelectric and the

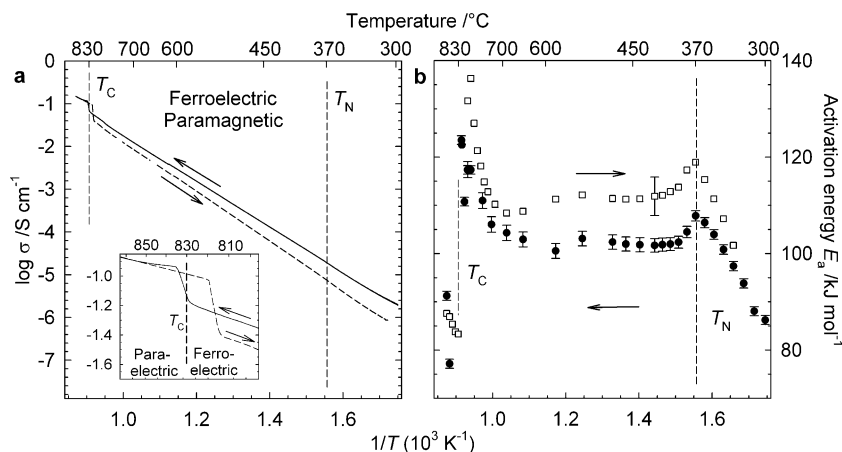


Figure 5. Electrical conductivity. a) $\log \sigma$ versus $1/T$ plot of electrical conductivity. Inset: conduction hysteresis associated with the ferroelectric transition. b) Activation energy E_a for conduction. Typical size of error bars is given for one data point for clarity.

paraelectric phase. The increased conductivity can be rationalized from the smaller unit cell volume and the higher symmetry of the $R\bar{3}c$ structure. The average activation energy E_a (Fig. 5b) of the electrical conductivity in the ferroelectric, paramagnetic region from 400 to 700 $^{\circ}\text{C}$ is 102 kJ mol^{-1} upon heating, and correspondingly 85 kJ mol^{-1} in the paraelectric phase above T_C . Neglecting any contribution from ionic conductivity and assuming intrinsic semiconductivity, the band gaps in ferroelectric, paramagnetic region, and the paraelectric region can be estimated from the relation $E_g = 2E_a k_B / eR$ to be 2.12 and 1.76 eV, respectively. This is not in agreement with band structure calculations^[11] and optical absorption measurements,^[17] pointing to a polaron hopping mechanism for the electronic conductivity. E_a calculated from the slope of the $\ln \sigma$ versus $1/T$ in 20 $^{\circ}\text{C}$ intervals shows an anomaly associated with the antiferromagnetic to paramagnetic transition. E_a increases close to linearly at low temperature in the antiferromagnetic phase to a maximum at the Néel temperature, followed by a decrease to the stable value in the temperature interval 400–700 $^{\circ}\text{C}$ in the paramagnetic phase. The effect is tentatively associated with spin frustration at the loss of magnetic order and the anomalous lattice expansion in the vicinity of T_N (Fig. 2a). The anomaly in the activation energy approaching T_C reflects the enhanced conductivity due to onset of the structural instability of the ferroelectric phase. The finite difference in conductivity and E_a upon heating and cooling is an anomaly of the experiment, possibly related to loss of electrode contact and microcracking of the sample due to the large $\Delta_{\text{trs}}V$, and interface reactions^[32] with the platinum electrodes. Post-measurement powder XRD of the crushed sample revealed no decomposition of the material.

In summary, the thermodynamic order and crystallographic nature of the ferroic phase transitions of BiFeO_3 has been identified. The paraelectric crystal structure has been identified as hexagonal (rhombohedral), with the centrosymmetric space group $R\bar{3}c$. The ferroelectric transition $R3c$ to $R\bar{3}c$ is an abrupt, first order transition of mainly displacive character with

significant $\Delta_{\text{trs}}V$ and $\Delta_{\text{trs}}H$. Rapid decrease in unit cell distortion and cation displacements at T_C is reflected by increased electronic conductivity. Near-isotropic lattice expansion and an anomaly in activation energy for electronic conduction is observed at T_N .

Experimental

Sample Preparation: Polycrystalline BiFeO_3 and powders of BiFeO_3 were prepared by solid-state reaction of Bi_2O_3 and Fe_2O_3 fired once at 825 $^{\circ}\text{C}$ for 8 h with a heating and cooling rate of 400 $^{\circ}\text{C h}^{-1}$. Additional material for confirming the paraelectric crystal structure was prepared by a chemical synthesis route. Details about the solid state and chemical synthesis can be found elsewhere. [33] The relative density of as-fired ceramic polycrystals was confirmed to be 95–98% by the Archimedes method, and powders were obtained by crushing the as-fired polycrystals in an agate mortar.

Calorimetry and Dilatometry: Differential thermal analysis was performed with a Netzsch STA 449 C Jupiter in synthetic air on powder (496 mg) and a dense polycrystal (584 mg) in alumina crucibles. The samples were heated to 880 $^{\circ}\text{C}$ with a rate of 10 $^{\circ}\text{C min}^{-1}$, held for 1 h at 880 $^{\circ}\text{C}$, before cooled to ambient temperature with a rate of 10 $^{\circ}\text{C min}^{-1}$. Differential scanning calorimetry was performed with a PerkinElmer DSC 7, PE Thermal Analysis Controller TAC 7/DX and Pyris v. 3.81 software. A 100 mg sample was encapsulated in an aluminum sample pan and the measurement was done with 40 $^{\circ}\text{C min}^{-1}$ heating and cooling rates. Thermal expansion of a dense polycrystalline sample from room temperature to 880 $^{\circ}\text{C}$ in air was measured with a Netzsch DIL 402 C dilatometer, using a heating rate of 2 $^{\circ}\text{C min}^{-1}$.

High Temperature X-Ray Diffraction: HTXRD was performed in air using a θ - θ Bruker AXS D8 ADVANCE diffractometer with a VANTEC-1 detector and a high temperature stage (mri Physikalische Geräte GmbH). Data acquisition was done with 3 s per step and a step size of 0.016 $^{\circ} 2\theta$ after holding for 30 min at each temperature to establish thermal equilibrium prior to measurement. Full temperature range measurements on powder was performed from 20 to 120 $^{\circ} 2\theta$, with a total time of 5.5 h scan $^{-1}$, and on a polycrystal in the vicinity of T_N from 20 to 96 $^{\circ} 2\theta$, with a total time of 4.2 h scan $^{-1}$. Temperature calibration was done using corundum powder. Estimated uncertainty of temperature calibration is ± 10 $^{\circ}\text{C}$. Additional HTXRD characterization of bulk powder close to T_C , and on wet chemically prepared powder above T_C , was done with a Siemens D5005 2θ - θ diffractometer with Cu $K\alpha$ radiation, a secondary monochromator and a HTK 16, Anton Paar GmbH high temperature camera.

Rietveld Refinement: The software TOPAS R (Bruker AXS, version 2.1) was used for Rietveld refinements. The space groups $R3c$ and $R\bar{3}c$ with hexagonal axes were used as the basis for the low and high temperature structures, respectively. Initial atomic positions were adopted from Fischer et al. [34]. Backgrounds were refined with sixth order Chebichev polynomials and peak profiles with Pearson VII functions. Isotropic temperature factors were refined, and a texture correction function was used for the polycrystalline sample. R_{wp} values varied from 4 (low temperature) to 7 (high temperature) for powders and close to 8 for all temperatures for the polycrystalline sample.

Electrical Conductivity Measurements: Conductivity was measured on a dense polycrystalline sample by a four-point technique enabling both current (I) and voltage (V) to be measured independently (Keithley D500). Two Pt electrodes were attached with Pt paste at each end of the sample, and an Al_2O_3 clamp pulled the sample down on two other Pt electrodes placed at a distance $d = 4.9$ mm apart. The conductivity (σ) was calculated from $\sigma = Id/UA$ where A is the area of

the cross-section normal to the current. The polycrystalline monolithic sample was polished with SiC paper to a cross-section of 0.2 cm^2 . The sample was placed inside a quartz tube and heated in a furnace to enable control of atmosphere and temperature. The measurements were performed in synthetic air with a heating rate of 3°C min^{-1} .

Received: January 23, 2008

Revised: May 26, 2008

Published online: August 27, 2008

- [1] a) G. A. Smolenskii, I. E. Chupis, *Sov. Phys. Usp.* **1982**, 25, 475. b) W. Eerenstein, N. D. Mathur, J. F. Scott, *Nature* **2006**, 442, 759.
- [2] a) N. A. Spaldin, M. Fiebig, *Science* **2005**, 309, 391. b) R. Ramesh, N. A. Spaldin, *Nat. Mater.* **2007**, 6, 21.
- [3] T. Lottermoser, T. Lonkai, U. Amann, D. Hohlwein, J. Ihringer, M. Fiebig, *Nature* **2004**, 430, 541.
- [4] T. Kimura, T. Goto, H. Shintani, K. Ishizaka, T. Arima, Y. Tokura, *Nature* **2003**, 426, 55.
- [5] M. Fiebig, *J. Phys. D: Appl. Phys.* **2005**, 38, R123.
- [6] F. Kubel, H. Schmid, *Acta Cryst.* **1990**, B46, 698.
- [7] J. M. Moreau, C. Michel, R. Gerson, W. J. James, *J. Phys. Chem. Solids* **1971**, 32, 1315.
- [8] J. R. Teague, R. Gerson, W. J. James, *Solid State Commun.* **1970**, 8, 1073.
- [9] J. Wang, J. B. Neaton, H. Zheng, V. Nagarajan, S. B. Ogale, B. Liu, D. Viehland, V. Vaithyanathan, D. G. Schlom, U. V. Waghmare, N. A. Spaldin, K. M. Rabe, M. Wuttig, R. Ramesh, *Science* **2003**, 299, 1719.
- [10] J. B. Neaton, C. Ederer, U. V. Waghmare, N. A. Spaldin, K. M. Rabe, *Phys. Rev. B* **2005**, 71, 014113.
- [11] P. Ravindran, R. Vidya, A. Kjekshus, H. Fjellvåg, O. Eriksson, *Phys. Rev. B* **2006**, 74, 224412.
- [12] a) J. Dho, X. Qi, H. Kim, J. L. MacManus-Driscoll, M. G. Blamire, *Adv. Mater.* **2006**, 18, 1445. b) Y.-H. Chu, Q. Zhan, L. W. Martin, M. P. Cruz, P.-L. Yang, G. W. Pabst, F. Zavaliche, S.-Y. Yang, J.-X. Zhang, L.-Q. Chen, D. G. Schlom, I.-N. Lin, T.-B. Wur, R. Ramesh, *Adv. Mater.* **2006**, 18, 2307. c) Y.-H. Chu, M. P. Cruz, C.-H. Yang, L. W. Martin, P.-L. Yang, J.-X. Zhang, K. Lee, P. Yu, L.-Q. Chen, R. Ramesh, *Adv. Mater.* **2007**, 19, 2662.
- [13] A. Palewicz, R. Przenioslo, I. Sosnowska, A. W. Hewat, *Acta Cryst.* **2007**, B63, 537.
- [14] M. Valant, A.-K. Axelsson, N. Alford, *Chem. Mater.* **2007**, 19, 5431.
- [15] R. Haumont, J. Kreisel, P. Bouvier, F. Hippert, *Phys. Rev. B* **2006**, 73, 132101.
- [16] A. Maître, M. François, J. C. Gachon, *J. Phase Equilib.* **2004**, 25, 59.
- [17] R. Palai, R. S. Katiyar, H. Schmid, P. Tissot, S. J. Clark, J. Robertson, S. A. T. Redfern, G. Catalan, J. F. Scott, *Phys. Rev. B* **2008**, 77, 014110.
- [18] I. A. Kornev, S. Lisenkov, R. Haumont, B. Dkhil, L. Bellaiche, *Phys. Rev. Lett.* **2007**, 99, 227602.
- [19] M. M. Kumar, V. R. Palkar, K. Srinivas, S. V. Suryanarayana, *Appl. Phys. Lett.* **2000**, 76, 2764.
- [20] J. D. Bucci, B. K. Robertson, W. J. James, *J. Appl. Cryst.* **1972**, 5, 187.
- [21] H. D. Megaw, C. N. W. Darlington, *Acta Cryst.* **1975**, A31, 161.
- [22] S. M. Selbach, T. Tybell, M.-A. Einarsrud, T. Grande, *Chem. Mater.* **2007**, 19, 6478.
- [23] S. Lee, A. Pirogov, J. H. Han, J.-G. Park, A. Hoshikawa, T. Kamiyama, *Phys. Rev. B* **2005**, 71, 180413(R).
- [24] B. B. van Aken, T. T. M. Palstra, A. Filippetti, N. A. Spaldin, *Nat. Mater.* **2004**, 3, 164.
- [25] A. M. Glazer, *Acta Cryst.* **1975**, A31, 756.
- [26] A. M. Glazer, *Acta Cryst.* **1972**, B28, 3384.
- [27] K. Kleveland, N. Orlovskaya, T. Grande, A. M. M. Moe, M.-A. Einarsrud, K. Breder, G. Gogotsi, *J. Am. Ceram. Soc.* **2001**, 84, 2029.
- [28] a) S. Kamba, D. Nuzhnyy, M. Savinov, J. Šebek, J. Petzelt, J. Prokleška, R. Haumont, J. Kreisel, *Phys. Rev. B* **2007**, 75, 024403. b) R. P. S. M. Lobo, R. L. Moreira, D. Lebeugle, D. Colson, *Phys. Rev. B* **2007**, 76, 172105.
- [29] P. Hermet, M. Goffinet, J. Kreisel, P. Ghosez, *Phys. Rev. B* **2007**, 75, 220102(R).
- [30] a) H. Boysen, F. Altorfer, *Acta Cryst.* **1994**, B50, 405. b) A. Hushur, S. Gvasaliya, B. Roessli, S. Lushnikov, S. Kojima, *Phys. Rev. B* **2007**, 76, 064104.
- [31] A. S. Chaves, F. C. S. Barreto, R. A. Nogueira, B. Zeks, *Phys. Rev. B* **1976**, 13, 207.
- [32] S. Yakovlev, J. Zekonyte, C.-H. Solterbeck, M. Es-Souni, *Thin Solid Films* **2005**, 493, 24.
- [33] S. M. Selbach, M.-A. Einarsrud, T. Tybell, T. Grande, *J. Am. Ceram. Soc.* **2007**, 90, 3430.
- [34] P. Fischer, M. Polomska, I. Sosnowska, M. Szymanski, *J. Phys. C: Solid State Phys.* **1980**, 13, 1931.